A full Stokes subgrid scheme in two dimensions for simulation of grounding line migration in ice sheets using Elmer/ICE (v8.3)

Gong Cheng[1], Per Lötstedt[1], and Lina von Sydow[1]

[1]Department of Information Technology, Uppsala University, P. O. Box 337, SE-75105 Uppsala, Sweden

Correspondence: Gong Cheng (cheng.gong@it.uu.se)

Abstract. The full Stokes equations are solved by a finite element method for simulation of large ice sheets and glaciers. The simulation is particularly sensitive to the discretization of the grounding line which separates the ice resting on the bedrock and the ice floating on water and is moving in time. The boundary conditions at the ice base are enforced by Nitsche's method and a subgrid treatment of the element in the discretization with the grounding line. Simulations with the method in two dimensions for an advancing and a retreating grounding line illustrate the performance of the method. The computed grounding line position is compared to previously published data with a fine mesh. Similar results are obtained using subgrid modeling with more than 20 times coarser meshes. It is implemented in the two dimensional version of the open source code Elmer/ICE.

1 Introduction

1.1 Ice sheet dynamics, sea-level rise, and grounding line migration

Simulation of ice sheet dynamics is a tool to assess the future sea-level rise (SLR) due to melting of continental ice sheets and glaciers (Hanna et al., 2013) and to reconstruct the ice sheets of the past (Stokes et al., 2015; DeConto and Pollard, 2016) for comparison with measurements and validation of the models. The predictions are particularly sensitive to the position of the grounding line (GL) and its numerical treatment (Durand and Pattyn, 2015; Konrad et al., 2018), the line where the ice sheet leaves the solid bedrock and becomes an ice shelf floating on water driven by buoyancy.

The distance that the GL moves may be long over palaeo time scales. In Kingslake et al. (2018) it is shown that the GL has retreated several hundred kilometers in West Antarctica during the last 11,500 years and then advanced again after the isostatic rebound of the bed. The sensitivity, long time intervals, and long distances require a careful treatment of the GL and its neighborhood by the numerical method to discretize the equations modeling the ice sheet dynamics. In this paper, we develop an accurate and efficient method for such problems.

1.2 Model equations

When the ice rests on the ground and is affected by frictional forces on the bed, the ice flow is dominated by vertical shear stresses when the basal friction is large. On the other hand, when the ice is floating on water, it is the longitudinal stress gradient

that controls the flow of the ice. The GL is in the transition zone between these two types of flow with a gradual change of the stress field (Schoof, 2011).

The most accurate ice model in theory is based on the full Stokes (FS) equations. A simplification of the FS equations by integrating in the depth of the ice is the shallow shelf (or shelfy stream) approximation (SSA) (MacAyeal, 1989). It is often used for simulation of the coupling between a grounded ice sheet and a marine ice shelf. In the zone between the grounded ice and the floating ice, it is necessary to use the FS equations (Wilchinsky and Chugunov, 2000; Schoof and Hindmarsh, 2010; Docquier et al., 2011; Schoof, 2011) unless the ice is moving rapidly on the ground with low basal friction, when the SSA equations are accurate both upstream and downstream of the GL.

The evolution of the GL in simulations is sensitive to the model equations and the basal friction law. In a major effort MISMIP (Pattyn et al., 2012, 2013), different ice models and implementations solve the same ice flow problems and the predicted GL steady state and transient GL motion are compared. The results show that the position of the GL depends on the model equations (Pattyn et al., 2013). The prediction of the GL and the SLR is different for different ice models such as FS and SSA (Pattyn and Durand, 2013). Including equations with vertical shear stress at the GL such as the FS equations seems to be crucial.

The friction laws at the ice base depend on the effective pressure, the basal velocity, and the distance to the GL in different combinations in Leguy et al. (2014); Gagliardini et al. (2015); Brondex et al. (2017); Gladstone et al. (2017). The GL position and the SLR vary considerably depending on the choice of friction law. Given the friction law, the results are sensitive to its model parameters too (Gong et al., 2017).

1.3 Numerical methods

Parameters in the numerical methods also influence the GL migration. It is observed in Durand et al. (2009b) that the mesh resolution along the ice bed has to be fine to obtain reliable solutions with FS in GL simulations. The GL is then located in a node of the fixed or static mesh. A mesh size below 1 km is necessary in Larour et al. (2019) to resolve the features at the GL. Adaptive meshes for a finite volume discretization of an approximation of the FS equations are employed in Cornford et al. (2013) to study the GL retreat and loss of ice in West Antarctica. The FS solutions of benchmark problems in Pattyn et al. (2013) computed by an implementation of the finite element method (FEM) in Elmer/ICE (Gagliardini et al., 2013) and FELIX-S (Leng et al., 2012) are compared in Zhang et al. (2017). The differences between the codes are attributed to different treatment of a friction parameter at the GL and different assignment of grounded and floating nodes and element faces.

A subgrid scheme introduces an inner structure in the discretization element or mesh volume where the GL is located. Such schemes have been developed for simplifications of the FS equations. A subgrid model for the GL is tested in Gladstone et al. (2010b) for the one dimensional (1D) SSA equation where the flotation condition for the ice defines the position of the GL. The GL migration is determined by the two dimensional (2D) SSA equations discretized by the finite element method (FEM) in Seroussi et al. (2014). Subgrid models at the GL are compared to a model without an internal structure in the element. The conclusion is that sub-element parameterization is necessary. A shallow approximation to FS with a subgrid scheme on coarse meshes is compared to FS in Feldmann et al. (2014) with similar results for the GL migration. Subgrid modeling and adaptivity

are compared in Cornford et al. (2016) for a vertically integrated model. The thickness of the ice above flotation determines if the ice is grounded or floating. A fine mesh resolution is necessary for converged GL positions with FS in Durand et al. (2009a, b). A dynamic mesh refinement and coarsening of the mesh following the GL would solve the problem in palaeo simulations when the GL moves long distances. An alternative is to introduce a subgrid scheme in the mesh elements where the GL is located in a static mesh and keep the mesh size coarser.

1.4 Our proposed method and outline of the paper

From the above we conclude that

- the prediction of SLR is very sensitive to the position of the GL and the numerical treatment in a neighbourhood of the GL,
- it seems crucial that the ice model includes equations with vertical shear stress in the neighbourhood of the GL,
- one way to avoid the fine meshes that are otherwise needed close to the GL, is to introduce a subgrid scheme in the discretization element where the GL is located.

For this purpose, we develop a numerical method for the FS equations in two dimensions introducing a subgrid scheme in the mesh element where the GL is located. Since the subgrid scheme is restricted to one element in a 2D vertical ice this is computationally inexpensive. In an extension to 3D, the subgrid scheme would be applied along a line of elements in 3D. The results with numerical modeling will always depend on the mesh resolution but can be more or less sensitive to the mesh spacing and time steps.

We solve the FS equations in a 2D vertical ice with the Galerkin method implemented in Elmer/ICE (Gagliardini et al., 2013). A subgrid discretization is proposed and tested for the element where the GL is located. The boundary conditions are imposed by Nitsche's method at the ice base in the weak formulation of the equations (Nitsche, 1971; Urquiza et al., 2014; Reusken et al., 2017). The linear Stokes equations are solved in Chouly et al. (2017a) with Nitsche's treatment of the boundary conditions. They solve the equations for the displacement but here we solve for the velocity using similar numerical techniques to weakly impose the Dirichlet boundary conditions on the normal velocity at the base. The frictional force in the tangential direction is applied on part of the element with the GL. The position of the GL within the element is determined in agreement with theory developed for the linearized FS in Schoof (2011).

The paper is organized as follows. Section 2 is devoted to the presentation of the mathematical model of the ice sheet dynamics. In Sect. 3, the numerical discretization with FEM is given while the subgrid scheme around the GL is found in Sect. 4. The numerical results for a MISMIP problem are presented in Sect. 5. The extension to three dimensions (3D) is discussed in Sect. 6 and finally some conclusions are drawn in Sect. 7.

2 Ice model

2.1 The full Stokes (FS) equations

We use the FS equations in a 2D vertical ice with coordinates $\mathbf{x} = (x, z)^T$ for modeling the flow of an ice sheet (Hutter, 1983). The nonlinear partial differential equations (PDEs) in the interior of the ice domain Ω are given by

$$\begin{cases} \nabla \cdot \mathbf{u} = 0, \\ -\nabla \cdot \sigma = \rho \mathbf{g}, \end{cases} \tag{1}$$

where the stress tensor is $\sigma = \tau(\mathbf{u}) - p\mathbb{I}$ and the deviatoric stress tensor is $\tau(\mathbf{u}) = 2\eta(\mathbf{u})\dot{\epsilon}(\mathbf{u})$. The strain rate tensor is defined by

$$\dot{\epsilon}(\mathbf{u}) = \frac{1}{2}(\nabla \mathbf{u} + \nabla \mathbf{u}^T) = \begin{pmatrix} \dot{\epsilon}_{11} & \dot{\epsilon}_{12} \\ \dot{\epsilon}_{12} & \dot{\epsilon}_{22} \end{pmatrix}, \tag{2}$$

$\mathbb{I}$ is the identity matrix, and the viscosity is defined by Glen's flow law

$$\eta(\mathbf{u}) = \frac{1}{2}\left(\mathcal{A}(T')\right)^{-\frac{1}{n}} \dot{\epsilon}_e^{\frac{1-n}{n}}, \qquad \dot{\epsilon}_e = \sqrt{\frac{1}{2}\mathrm{tr}(\dot{\epsilon}(\mathbf{u})\dot{\epsilon}(\mathbf{u}))}. \tag{3}$$

Here $\mathbf{u} = (u, w)^T$ is the vector of velocities, ρ is the density of the ice, p denotes the pressure, and the gravitational vector is denoted by $\mathbf{g}$. The viscosity η is a function of the rate factor $\mathcal{A}(T')$ where T' is the ice temperature. For isothermal flow assumed here, the rate factor $\mathcal{A}$ is constant. Finally, n is usually taken to be 3.

2.2 Boundary conditions

At the boundary Γ of the ice domain Ω we define the normal outgoing vector $\mathbf{n}$ and tangential vector $\mathbf{t}$ (see Fig. 1). In the 2D vertical case considered here, the ice sheet geometry is constant in y. The ice surface is denoted by Γ_s and the ice base is $\Gamma_b = \Gamma_{bg} \cup \Gamma_{bf}$. At Γ_s and Γ_{bf}, the floating part of Γ_b, we have that

$$\sigma \mathbf{n} = \mathbf{f}_s \quad , \quad \sigma \mathbf{n} = \mathbf{f}_{bf}, \tag{4}$$

respectively. The ice is stress-free at Γ_s, $\mathbf{f}_s = 0$, and $\mathbf{f}_{bf} = -p_w \mathbf{n}$ at the ice/ocean interface Γ_{bf} where p_w is the water pressure. Let

$$\sigma_{\mathbf{nt}} = \mathbf{t} \cdot \sigma \mathbf{n},\ \sigma_{\mathbf{nn}} = \mathbf{n} \cdot \sigma \mathbf{n},\ u_{\mathbf{t}} = \mathbf{t} \cdot \mathbf{u},$$

where $\boldsymbol{\sigma}_{\mathbf{nn}}$ and $\boldsymbol{\sigma}_{\mathbf{nt}}$ are the normal and tangential components of the stress and $u_{\mathbf{t}}$ is the tangential component of the ice velocity at the ice base. Then for the slip boundary Γ_{bg}, the grounded part of Γ_b where the ice rests on the bedrock, we have a friction law for the sliding ice

$$\sigma_{\mathbf{nt}} + \beta(\mathbf{u}, \mathbf{x}) u_{\mathbf{t}} = 0, \quad u_{\mathbf{n}} = \mathbf{n} \cdot \mathbf{u} = 0, \quad -\sigma_{\mathbf{nn}} \geq p_w, \tag{5}$$

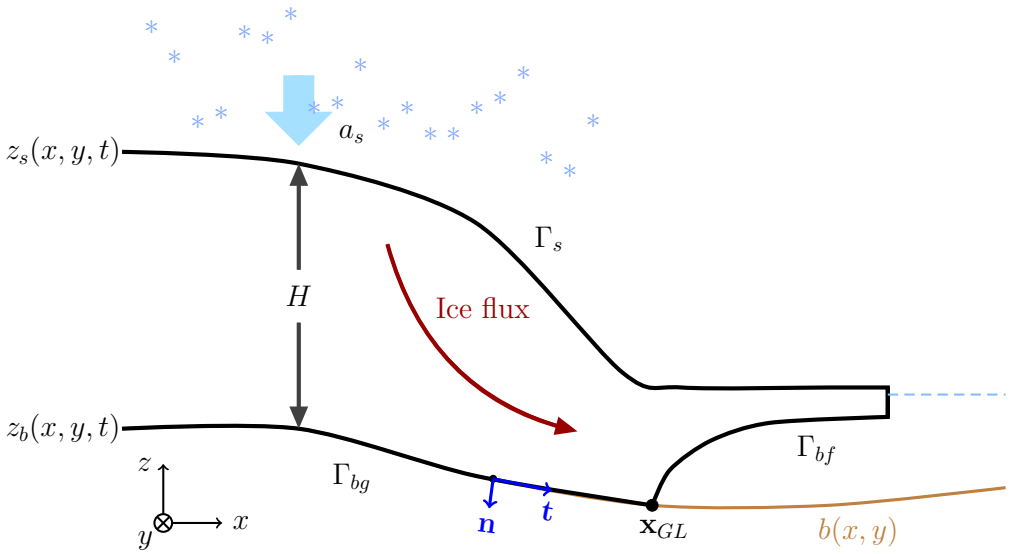

Figure 1. A two dimensional schematic view of a marine ice sheet.

where $u_\mathbf{n}$ is the normal component of the ice velocity. The type of friction law is determined by the friction coefficient β (≥ 0). At Γ_{bf}, there is a balance between $\sigma_{\mathbf{nn}}$ and p_w and the contact is friction-free, $\beta = 0$. Then

$$\sigma_{\mathbf{nt}} = 0, \qquad -\sigma_{\mathbf{nn}} = p_w. \tag{6}$$

At the GL, the boundary condition switches from $\beta > 0$ and $u_\mathbf{n} = 0$ on Γ_{bg} to $\beta = 0$ and a free $u_\mathbf{n}$ on Γ_{bf}. In a 2D vertical ice, the GL is the point (x_{GL}, z_{GL}) shared between Γ_{bg} and Γ_{bf}.

The ocean surface is at $z = 0$, and $p_w = -\rho_w g z_b$. The density of sea water is denoted byρ_w, z_b is the z-coordinate of Γ_b, and g is the vertical component of the gravitational force.

2.3 The free surface equations

The boundaries Γ_s and Γ_b are time-dependent and move according to two free surface equations. The boundary Γ_{bg} follows the fixed bedrock with coordinates $(x, b(x))$.

The z-coordinate of the ice surface position $z_s(x,t)$ at Γ_s (see Fig. 1) is the solution of an advection equation

$$\frac{\partial z_s}{\partial t} + u_s \frac{\partial z_s}{\partial x} - w_s = a_s, \tag{7}$$

where a_s denotes the surface mass balance and $\mathbf{u}_s = (u_s, w_s)^T$ the velocity at the ice surface in contact with the atmosphere. Similarly, the z-coordinate for the ice base z_b of the floating ice at Γ_{bf} satisfies

$$\frac{\partial z_b}{\partial t} + u_b \frac{\partial z_b}{\partial x} - w_b = a_b, \tag{8}$$

where a_b is the basal mass balance and $\mathbf{u}_b = (u_b, w_b)^T$ the velocity of the ice at Γ_{bf}. On Γ_{bg}, $z_b = b(x)$ and on Γ_{bf}, $z_b > b(x)$.

The thickness of the ice is denoted by $H = z_s - z_b$ and depends on x and t.

2.4 A first order solution close to the grounding line

The 2D vertical solution of the FS equations in Eq. (1) with a constant viscosity, $n = 1$ in Eq. (3), is expanded in small parameters in Schoof (2011). The solutions in different regions around the GL are connected by matched asymptotics. Upstream of the GL at the grounded part, $x < x_{GL}$, the leading terms in the expansion satisfy a simple relation in scaled variables close to the GL. Across the GL, the ice velocity u, the flux of ice uH, and the depth integrated normal or longitudinal stress τ_{11} in Eq. (2) are continuous. By including higher order terms in the expansion in small parameters, it is shown in Schoof (2011, Sect. 4.7) that the ice surface slope is continuous and Archimedes' flotation condition

$$H\rho = -z_b\rho_w \tag{9}$$

is not satisfied immediately downstream of the GL. A rapid variation in the vertical velocity w in a short distance interval at the GL causes oscillations in the ice surface in the analysis as also observed in FS simulations in Durand et al. (2009a). The flotation condition in (9) determines where the GL is in SSA in Docquier et al. (2011); Drouet et al. (2013).

In Schoof (2011, Sect. 4.3), the solution to the FS in a 2D vertical ice is expanded in two parameters, ν and ϵ. The aspect ratio of the ice ν is the quotient between a typical scale of the thickness of the ice $\mathcal{H}$ and a horizontal length scale $\mathcal{L}$, $\nu = \mathcal{H}/\mathcal{L}$, and ϵ is ν times the quotient between the longitudinal and the shear stresses τ_{11} and τ_{12} in Eq. (2). If $\nu^{5/2} \ll \epsilon \ll 1$ then in a boundary layer close to the GL and $x < x_{GL}$ it follows from the equations that the leading terms in the solution in scaled variables satisfy

$$\tau_{22} - p = \sigma_{22} = \rho g(z - z_s). \tag{10}$$

On floating ice $\tau_{22} - p + p_w = 0$ and the hydrostatic flotation criterion Eq. (9) is fulfilled. This is a first order approximation of the second relation in Eq. (6). On the grounded ice domain, we have $\tau_{22} - p + p_w < 0$.

Introducing the notation

$$\chi_a(x, z) = \tau_{22} - p + p_w = \rho g(z - z_s(x)) - \rho_w g z_b(x), \tag{11}$$

and letting $H_{bw} = -z_b$ be the thickness of the ice below the sea level yields

$$\chi_a(x, z_b) = -g(\rho H - \rho_w H_{bw}). \tag{12}$$

If $x < x_{GL}$ then $\chi_a < 0$ in the neighborhood of x_{GL} on Γ_{bg} and if $x > x_{GL}$ then $\chi_a = 0$ and Eq. (9) holds true on Γ_{bf}. Suppose that z_s and z_b are linear in x. Then χ_a is also linear in x. In numerical experiments with the linear FS $(n = 1)$ in Nowicki and Wingham (2008), $\chi_a(x, z_b)$ varies linearly in x for $x < x_{GL}$.

In Sect. 4, we mimic the same idea but use an indicator $\chi(x)$ or $\tilde{\chi}(x)$ derived from the solutions of the nonlinear FS equations to estimate the GL position. These indicators are approximated by $\chi_a(x, z_b)$.

3 Discretization by FEM

In this section we state the weak form of Eq. (1) and introduce the spatial FEM discretization used for Eq. (1) and give the time-discretization of Eq. (7) and (8).

3.1 The weak form of the FS equations

We start by defining the mixed weak form of the FS equations. Introduce $k = 1+1/n$, $k^* = 1+n$ with n from Glen's flow law and the spaces

$$\boldsymbol{V}_k = \{\mathbf{v} : \mathbf{v} \in (W^{1,k}(\Omega))^2\}, \quad Q_{k^*} = \{q : q \in L^{k^*}(\Omega)\}, \tag{13}$$

see, e.g. Jouvet and Rappaz (2011, Eq. (3.7)), Chen et al. (2013, Sect. 3.1), Martin and Monnier (2014, Eq. (21)). The weak solution $(\mathbf{u},p)$ of Eq. (1) is obtained as follows. Find $(\mathbf{u},p) \in \boldsymbol{V}_k \times Q_{k^*}$ such that for all $(\mathbf{v},q) \in \boldsymbol{V}_k \times Q_{k^*}$ the equation

$$A((\mathbf{u},p),(\mathbf{v},q)) + B_\Gamma(\mathbf{u},\mathbf{v},p) + B_\mathcal{N}(\mathbf{u},\mathbf{v},q) = F(\mathbf{v}) + F_\Gamma(\mathbf{v}), \tag{14}$$

is satisfied, where

$$A((\mathbf{u},p),(\mathbf{v},q)) = \int_\Omega 2\eta(\mathbf{u})\dot{\epsilon}(\mathbf{u}) : \dot{\epsilon}(\mathbf{v}) \ \mathrm{d}\mathbf{x} - b(\mathbf{u},q) - b(\mathbf{v},p),$$

$$b(\mathbf{u},q) = \int_\Omega q \nabla\cdot\mathbf{u} \ \mathrm{d}\mathbf{x},$$

$$B_\Gamma(\mathbf{u},\mathbf{v},p) = -\int_{\Gamma_{bg}} (\sigma_{\mathbf{nn}}(\mathbf{u},p)\mathbf{n}\cdot\mathbf{v} + \sigma_{\mathbf{nt}}(\mathbf{u},p)\mathbf{t}\cdot\mathbf{v}) \ \mathrm{d}s = \int_{\Gamma_{bg}} (-\sigma_{\mathbf{nn}}(\mathbf{u},p)\mathbf{n}\cdot\mathbf{v} + \beta(\mathbf{t}\cdot\mathbf{u})(\mathbf{t}\cdot\mathbf{v})) \ \mathrm{d}s,$$

$$B_\mathcal{N}(\mathbf{u},\mathbf{v},q) = -\int_{\Gamma_{bg}} \sigma_{\mathbf{nn}}(\mathbf{v},q)\mathbf{n}\cdot\mathbf{u} \, \mathrm{d}s + \gamma_0 \int_{\Gamma_{bg}} \frac{1}{h}(\mathbf{n}\cdot\mathbf{u})(\mathbf{n}\cdot\mathbf{v}) \, \mathrm{d}s,$$

$$F(\mathbf{v}) = \int_\Omega \rho\mathbf{g}\cdot\mathbf{v} \ \mathrm{d}\mathbf{x},$$

$$F_\Gamma(\mathbf{v}) = -\int_{\Gamma_{bf}} p_w \mathbf{n}\cdot\mathbf{v} \ \mathrm{d}s$$

The last term in $B_\mathcal{N}$ is added in the weak form in Nitsche's method (Nitsche, 1971) to impose the Dirichlet condition $u_\mathbf{n} = 0$ weakly on Γ_{bg}. It can be considered as a penalty term. Since $\mathbf{u} = u_\mathbf{n}\mathbf{n} + u_\mathbf{t}\mathbf{t}$, the contribution of the tangential force can also be written $\beta\mathbf{u}\cdot\mathbf{v}$ when $u_\mathbf{n} = 0$. The value of the positive parameter γ_0 depends on the physical problem and h is a measure of the mesh size on Γ_b. The sensitivity of the GL positions for different values of γ_0 is shown in Sect. 5. The first term in $B_\mathcal{N}$ symmetrizes the boundary term $B_\Gamma + B_\mathcal{N}$ on Γ_{bg} and vanishes when $u_\mathbf{n} = 0$. The boundary term $F_\Gamma(\mathbf{v})$ is from the buoyancy force at the ice/ocean interface in (6) where p_w depends on z_b on Γ_{bf}.

3.2 The discretized FS equations

We employ linear Lagrange elements with Galerkin Least Square (GLS) stabilization (Franca and Frey, 1992; Helanow and Ahlkrona, 2018) to avoid spurious oscillations in the pressure using the standard setting in Elmer/ICE (Gagliardini et al., 2013) approximating solutions in the spaces $\boldsymbol{V}_k$ and Q_{k^*} in Eq. (13).

The mesh is constructed from a footprint mesh on the ice base and then extruded with the same number of layers equidistantly in the vertical direction according to the thickness of the ice sheet. To simplify the implementation in 2D, the footprint mesh on the ice base consists of $N+1$ nodes at $\mathbf{x}_i = (x_i, z_b(x_i))$, $i = 0, \ldots, N$, with x-coordinates x_i and a constant mesh size $\Delta x = x_i - x_{i-1}$.

In general, the GL is somewhere in the interior of an interval $[x_{i-1}, x_i]$ and it crosses the interval boundaries as it moves forward in the advance phase and backward in the retreat phase of the ice. The advantage with Nitsche's way of formulating the boundary conditions is that if $x_{GL} \in [x_{i-1}, x_i]$ then the boundary integral over the interval can be split into two parts in Eq. (14) such that $(x, z_b(x)) \in \Gamma_{bg}$ when $x \in [x_{i-1}, x_{GL}]$ and if $x \in [x_{GL}, x_i]$ then $(x, z_b(x)) \in \Gamma_{bf}$. In the GL element, we have

$$
\begin{aligned}
B_\Gamma + B_\mathcal{N} &= \int\limits_{[x_{i-1}, x_{GL}]} -(\sigma_{\mathbf{nn}}(\mathbf{u}, p)\mathbf{n}\cdot\mathbf{v} + \sigma_{\mathbf{nn}}(\mathbf{v}, q)\mathbf{n}\cdot\mathbf{u}) + \beta(\mathbf{t}\cdot\mathbf{u})(\mathbf{t}\cdot\mathbf{v}) + \frac{\gamma_0}{h}(\mathbf{n}\cdot\mathbf{u})(\mathbf{n}\cdot\mathbf{v})\ \mathrm{d}s, \\
F_\Gamma &= -\int\limits_{[x_{GL}, x_i]} p_w \mathbf{n}\cdot\mathbf{v}\ \mathrm{d}s,
\end{aligned}
\tag{15}
$$

with the integration element $\mathrm{d}s$ following Γ_b. There is a change of the boundary condition in the middle of the FEM element where the GL is located. With a strong formulation of the boundary condition $u_\mathbf{n} = 0$, the basis functions in $\boldsymbol{V}_k$ share this property and the condition changes from the grounded node x_{i-1} where the basis function satisfies $u_\mathbf{n} = 0$ to the floating node at x_i with a free $u_\mathbf{n}$ without taking the position of the GL inside $[x_{i-1}, x_i]$ into account. With the weak formulation in Nitsche's method, the standard basis functions we use do not satisfy $u_\mathbf{n} = 0$ strictly. The boundary condition is imposed on the solution by the additional penalty term in (14) and this term may change inside an element as in (15).

The resulting system of nonlinear equations form a nonlinear complementarity problem (Christensen et al., 1998). The distance d between the base of the ice and the bedrock at time t and at x is

$$
d(x,t) = z_b(x,t) - b(x) \geq 0. \tag{16}
$$

If $d > 0$ on Γ_{bf} then the ice is not in contact with the bedrock and $\sigma_{\mathbf{nn}} + p_w = 0$ and if $\sigma_{\mathbf{nn}} + p_w < 0$ on Γ_{bg} then the ice and the bedrock are in contact and $d = 0$. Hence, the complementarity relation in the vertical direction is

$$
d(x,t) \geq 0,\ \sigma_{\mathbf{nn}} + p_w \leq 0, \quad d(x,t)(\sigma_{\mathbf{nn}} + p_w) = 0 \text{ on } \Gamma_b. \tag{17}
$$

The contact friction law is such that $\beta > 0$ when $x < x_{GL}$ and $\beta = 0$ when $x > x_{GL}$. The complementarity relation along the ice base at x is then the non-negativity of d and

$$
\beta \geq 0,\ \beta(x,t)d(x,t) = 0 \text{ on } \Gamma_b. \tag{18}
$$

In particular, these relations are valid at the nodes $x = x_j$, $j = 0, 1, \ldots, N$.

The complementarity condition also holds for $u_{\mathbf{n}}$ and $\sigma_{\mathbf{nn}}$ such that

$$\sigma_{\mathbf{nn}} + p_w \leq 0, \quad u_{\mathbf{n}}(\sigma_{\mathbf{nn}} + p_w) = 0 \text{ on } \Gamma_b, \tag{19}$$

without any sign constraint on $u_{\mathbf{n}}$ except for the retreat phase when the ice leaves the ground and $u_{\mathbf{n}} < 0$.

Similar implementations for contact problems using Nitsche's method are found in Chouly et al. (2017a, b), where the unknowns in the PDEs are the displacement fields instead of the velocity in Eq. (1). Analysis in Chouly et al. (2017a) suggests that Nitsche's method for the contact problem can provide a stable numerical solution with an optimal convergence rate.

The nonlinear equations, Eq. (14), for the nodal values of $\mathbf{u}$ and p are solved by Picard iterations. The system of linear equations in every Picard iteration is solved directly by using the MUMPS linear solver in Elmer/ICE. The condition on $d_j = d(x_j)$ is used to decide if the node x_j is geometrically grounded or floating. It is computed at each time step and is not changed during the nonlinear iterations (Picard). The procedure for solution of the nonlinear FS equations is outlined in Algorithm 1. In two dimensions, the GL will be located in one element.

Algorithm 1 Solve the FS equations

For a given mesh, compute $d_j, j = 0, 1, ..., N$, for all the nodes x_j at the ice base.
Mark node j as geometrically grounded if $d_j < 10^{-3}$, otherwise floating.
Find the element which contains both geometrically grounded and floating nodes, and mark the grounded node in this element as 'GL node'.
Compute the residual of the FS equations with the initial guess of the solution.
while the residual is larger than the tolerance **do**
  Assemble the FEM matrix for the interior of the domain Ω.
  for the boundary elements on Γ_b **do**
    if has 'GL node' **then**
      Mark the current element as a 'potential GL element'.
      Use the subgrid scheme in Algorithm 3 of Sect. 4 for the assembly.
    else
      Assemble the boundary element.
    end if
  end for
  Solve the linearized FS equations for a correction of the solution.
  Compute the solution and the residual.
end while

3.3 Discretization of the advection equations

The advection equations for the moving ice boundary in Eq. (7) and (8) are discretized in time by a finite difference method and in space by FEM with linear Lagrange elements for z_s and z_b. An artificial diffusion stabilization term is added, making the spatial discretization behave like an upwind scheme in the direction of the velocity as implemented in Elmer/ICE.

The advection equations Eq. (7) and Eq. (8) are integrated in time by a semi-implicit method of first order accuracy. Let $c = s$ or b. Then the solution is advanced from time t^ℓ to $t^{\ell+1} = t^\ell + \Delta t$ with the time step Δt by

$$z_c^{\ell+1} = z_c^\ell + \Delta t(a_c^\ell - u_c^\ell \frac{\partial z_c^{\ell+1}}{\partial x} + w_c^\ell). \tag{20}$$

The spatial derivative of z_c is approximated by FEM as described above. A system of linear equations is solved at $t^{\ell+1}$ for $z_c^{\ell+1}$. This time discretization and its properties are discussed in Cheng et al. (2017) and summarized in Algorithm 2.

Algorithm 2 Time scheme of the GL migration problem

Start from an initial geometry Ω^0 defined by z_b^0, z_s^0.
for $\ell = 0$ to $T/\Delta t - 1$ **do**
  Solve the FS equations on Ω^ℓ with Algorithm 1, to get the solution $\mathbf{u}^\ell$.
  Solve for $z_b^{\ell+1}$ and $z_s^{\ell+1}$ with $\mathbf{u}^\ell$ by the semi-implicit Euler method.
  Use $z_b^{\ell+1}$ and $z_s^{\ell+1}$ to update $\Omega^{\ell+1}$.
end for

A numerical stability problem in z_b is encountered in the boundary condition at Γ_{bf} when the FS equations are solved in Durand et al. (2009a). It is resolved by expressing z_b in p_w at Γ_{bf} with a damping term. An alternative interpretation of the idea in Durand et al. (2009a) and an explanation follow below.

The relation between $u_\mathbf{n}$ and $u_\mathbf{t}$ at Γ_{bf} and $\mathbf{u}_b = \mathbf{u}(x, z_b(x))$ is

$$\mathbf{u}_b = \begin{pmatrix} u_b \\ w_b \end{pmatrix} = \begin{pmatrix} z_{bx} \\ -1 \end{pmatrix} \frac{u_\mathbf{n}}{\sqrt{1+z_{bx}^2}} + \begin{pmatrix} 1 \\ z_{bx} \end{pmatrix} \frac{u_\mathbf{t}}{\sqrt{1+z_{bx}^2}}, \tag{21}$$

where z_{bx} denotes $\partial z_b/\partial x$. Inserting u_b and w_b from Eq. (21) into Eq. (8) yields

$$\frac{\partial z_b}{\partial t} = a_b - u_\mathbf{n}\sqrt{1+z_{bx}^2}. \tag{22}$$

Instead of discretizing Eq. (22) explicitly at $t^{\ell+1}$ with $u_\mathbf{n}^\ell$ to determine $p_w^{\ell+1}$, the base coordinate is updated implicitly

$$z_b^{\ell+1} = z_b^\ell + \Delta t\left(a_b^{\ell+1} - u_\mathbf{n}^{\ell+1}\sqrt{1+(z_{bx}^{\ell+1})^2}\right) \tag{23}$$

in the evaluation of p_w in $F_\Gamma(\mathbf{v})$ in Eq. (14).

Assuming that z_{bx} is small, the time step restriction in Eq. (23) is estimated by considering a 2D slab of the floating ice of width Δx and thickness H. Newton's law of motion yields

$$M\dot{u}_\mathbf{n} = Mg - \Delta x p_w,$$

where $M = \Delta x(z_s - z_b)\rho$ is the mass of the slab. Dividing by M, integrating in time for $u_{\mathbf{n}}(t^m)$, letting $m = \ell + 1$ or ℓ, and approximating the integral by the trapezoidal rule for the quadrature yields

$$u_{\mathbf{n}}(t^m) = \int_0^{t^m} g + \frac{g\rho_w}{\rho}\frac{z_b}{z_s - z_b}\,\mathrm{d}s \approx gt^m + \frac{g\rho_w}{\rho}\sum_{i=0}^{m}\alpha_i\frac{z_b^i}{z_s^i - z_b^i}\Delta t = u_{\mathbf{n}}^m,$$

with the parameters

$$\alpha_i = 0.5,\ i = 0, m, \quad \alpha_i = 1,\ i = 1, \ldots, m-1.$$

Then insert $u_{\mathbf{n}}^m$ into Eq. (23). All terms in $u_{\mathbf{n}}^m$ from time steps $i < m$ are collected in the sum $\Delta t F^{m-1}$. Then Eq. (23) can be written

$$z_b^{\ell+1} = z_b^\ell - \Delta t^2\frac{g\rho_w}{2\rho}\frac{z_b^m}{z_s^m - z_b^m} + \Delta t\left(a_b^\ell - gt^m - \Delta t F^{m-1}\right). \tag{24}$$

For small changes in z_b in Eq. (24), the explicit method with $m = \ell$ is stable when Δt is so small that

$$|1 - \Delta t^2\frac{g\rho_w}{2H\rho}| \le 1. \tag{25}$$

When $H = 100$ m on the ice shelf, $\Delta t < 6.1$ s which is far smaller than the stable steps for Eq. (20). Choosing the implicit scheme with $m = \ell + 1$, the bound on Δt is

$$1/|1 + \Delta t^2\frac{g\rho_w}{2H\rho}| \le 1, \tag{26}$$

i.e. there is no bound on positive Δt for stability but accuracy will restrict Δt.

Much longer stable time steps are possible at the surface and the base of the ice with a semi-implicit method Eq. (20) and a fully implicit method Eq. (23) compared to an explicit method. For example, the time step for the problem in Eq. (20) with 1 km mesh size can be up to a couple of months. Therefore, we use the scheme in Eq. (20) for Eqs. (7) and (8) and the scheme in Eq. (23) for Eq. (22) and p_w as in Durand et al. (2009a). The difference between the approximations of z_b in Eq. (20) and (23) is of $\mathcal{O}(\Delta t^2)$.

4 Subgrid scheme around the grounding line

The basic idea of the subgrid scheme for the FS equations in this paper follows the GL parameterization (SEP3) for SSA in Seroussi et al. (2014) and the analysis for FS in Schoof (2011). The GL is located at the position where the ice is on the ground and the flotation criterion is perfectly satisfied such that $\sigma_{\mathbf{nn}} = -p_w$. In the FS equations, the hydrostatic assumption Eq. (9) may not be valid close to the GL. Therefore, the GL position can not be determined by simply checking the total thickness of the ice H against the depth below sea level H_{bw}. Instead, the flotation criterion is computed by comparing the water pressure with the numerical normal stress component orthogonal to the boundary inspired by the first order analysis in Sect. 2.4.

The numerical solutions, e.g. Gagliardini et al. (2016); Gladstone et al. (2017), converge to the analytical solution of the FS PDE as the mesh size decreases. The analytical solution satisfies $z_b(x,t) > b(x)$ with the boundary conditions in Eq. (6) at the

base of the floating ice, and where the ice is in contact with the bedrock $z_b(x,t) = b(x)$, the boundary conditions are given by Eq. (5). Examples of the analytical solution are demonstrated by the thin light blue lines in Figs. 2 and 3 with a black '$*$' at the analytical GL position $\mathbf{x}_{GL}$. The two figures share the same analytical solution. However, as illustrated in Figs. 2 and 3, the basal boundary of the ice $z_b(x,t)$ does not conform with the mesh from the spatial discretization. In particular, the GL position $\mathbf{x}_{GL}$ of the analytical solution does not coincide with any of the nodes, but it usually stays on the bedrock $b(x)$ between the last grounded ($\mathbf{x}_{i-1}$) and the first floating ($\mathbf{x}_i$) nodes, see Figs. 2 and 3. The linear element boundary between any $\mathbf{x}_{j-1}$ and $\mathbf{x}_j$ is denoted by $\mathcal{E}_j$. The sequence of $\mathcal{E}_j, j = 1, \ldots, N$, approximates Γ_b. The grounding line element containing the GL is $\mathcal{E}_i$.

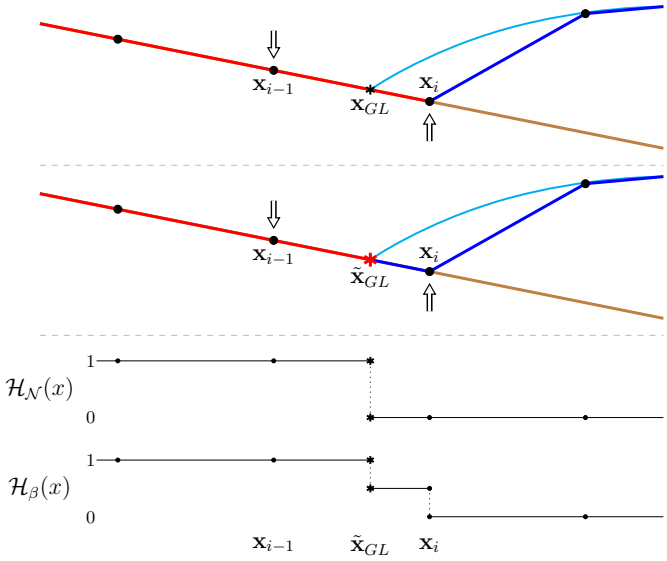

Figure 2. Schematic figure of the GL in case i, with the arrows indicating the direction of the net forces in the vertical direction. Upper panel: The last grounded and first floating nodes as defined in Elmer/ICE. The light blue line is the analytical solution of the ice sheet with the analytical GL position $\mathbf{x}_{GL}$. Middle panel: Linear interpolation to approximate the numerical GL position $\tilde{\mathbf{x}}_{GL}$. Lower panel: The step functions $\mathcal{H}_{\mathcal{N}}(x)$ and $\mathcal{H}_{\beta}(x)$ indicate the area for Nitsche's penalty and slip boundary conditions.

Depending on how the mesh is created from the initial geometry and updated during the simulation, the first floating node at $\mathbf{x}_i$, as well as the GL element, can be either on the bedrock (as in Fig. 2) or at the ice base above the bedrock (as in Fig. 3), even though the corresponding analytical solutions are identical. Denote the situation in Fig. 2 as case i, and the one in Fig. 3 as case ii. The physical boundary conditions of the two cases are different only at the GL element. More precisely, in case i, the net force in the vertical direction on the node $\mathbf{x}_i$ is pointing inward, namely $\chi(\mathbf{x}_i) = \sigma_{\mathbf{nn}}(\mathbf{x}_i) + p_w(\mathbf{x}_i) > 0$, whereas in case ii, the floating condition $\sigma_{\mathbf{nn}}(\mathbf{x}_i) + p_w(\mathbf{x}_i) = 0$ is satisfied in the node $\mathbf{x}_i$. The directions of the vertical net force at the nodes $\mathbf{x}_{i-1}$ and $\mathbf{x}_i$ are shown by the arrows in the upper panels of Fig. 2 and 3. Consequently, the external forces and boundary conditions imposed on the GL element are different in the two cases. For instance, in case i, the GL element is considered as geometrically grounded (defined as in Algorithm 1), shown with red color in the upper panel of Fig. 2. In case ii, the GL element is treated as geometrically floating and colored in blue in the upper panel of Fig. 3.

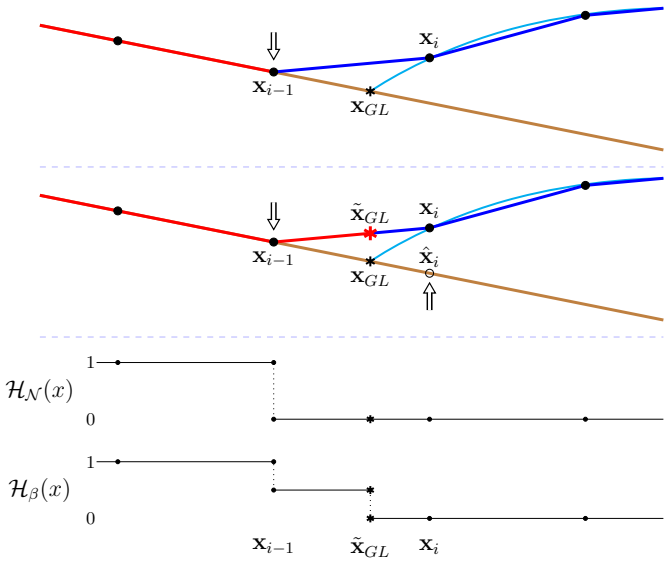

Figure 3. Schematic figure of the GL in case ii, with the arrows indicating the direction of the net forces in the vertical direction. Upper panel: The last grounded and first floating nodes as defined in Elmer/ICE. The light blue line is the analytical solution of the ice sheet with the analytical GL position $\mathbf{x}_{GL}$. The node $\mathbf{x}_i$ is fully geometrically floating and the net force is 0. Middle panel: Linear interpolation to approximate the numerical GL position $\tilde{\mathbf{x}}_{GL}$. The point $\hat{\mathbf{x}}_i$ on the bedrock has the same x coordinate as $\mathbf{x}_i$. Lower panel: The step functions $\mathcal{H}_{\mathcal{N}}(x)$ and $\mathcal{H}_{\beta}(x)$ indicate the area for Nitsche's penalty and slip boundary conditions.

These two cases are similar to the LG and FF cases in Gagliardini et al. (2016) implying that the numerical solutions in the two cases are different, especially on a coarse mesh (mesh size at about 100 m or larger). Thus, we propose a subgrid scheme to reduce these differences in the spatial discretization and to capture the GL migration without using a fine mesh resolution (< 100 m). The schematic drawing of the subgrid scheme for the two cases is shown in the middle panels of Fig. 2 and 3. The GL element is divided into the grounded (red) and floating (blue) parts by the estimated GL position $\tilde{\mathbf{x}}_{GL}$ on $\mathcal{E}_i$, which is the numerical approximation of the analytical GL position $\mathbf{x}_{GL}$.

The GL moves toward the ocean in the advance phase and away from the ocean in the retreat phase. First, we consider case i in the *advance phase* and define the indicator by

$$\chi(\mathbf{x}) = \sigma_{\mathbf{nn}} + p_w, \tag{27}$$

which vanishes on the floating ice and is negative and approximately equal to $\chi_a = \tau_{22} - p + p_w$ in Eq. (11) on the ground since the slope of the bedrock is small and $\mathbf{n} \approx (0, -1)^T$. Because of the poor spatial resolution of the coarse mesh, $\chi(\mathbf{x}_i)$ is positive.

To determine the position $\tilde{\mathbf{x}}_{GL}$, we solve $\chi(\tilde{\mathbf{x}}_{GL}) = \sigma_{\mathbf{nn}}(\tilde{\mathbf{x}}_{GL}) + p_w(\tilde{\mathbf{x}}_{GL}) = 0$ by linear interpolation between $\chi(\mathbf{x}_{i-1})$ and $\chi(\mathbf{x}_i)$ such that

$$\tilde{\mathbf{x}}_{GL} = \mathbf{x}_{i-1} - \frac{\chi(\mathbf{x}_{i-1})}{\chi(\mathbf{x}_{i-1}) - \chi(\mathbf{x}_i)}(\mathbf{x}_{i-1} - \mathbf{x}_i). \tag{28}$$

The water pressure $p_w(\mathbf{x})$ is a linear function of $\mathbf{x}$ on the GL element and the numerical solution of $\sigma_{\mathbf{nn}}(\mathbf{x})$ is also piecewise linear on every element with the standard Lagrange elements in Elmer/ICE (Gagliardini et al., 2013). Hence, it makes sense to approximate the analytical GL position $\mathbf{x}_{GL}$ by $\tilde{\mathbf{x}}_{GL}$ by linear interpolation in the current framework. This approach fits well with case i since the indicator $\chi(\mathbf{x})$ has opposite signs at $\mathbf{x}_{i-1}$ and $\mathbf{x}_i$, see the middle panel of Fig. 2 where $\tilde{\mathbf{x}}_{GL}$ is marked by a red '$*$'. It guarantees the existence and uniqueness of $\tilde{\mathbf{x}}_{GL}$ on the GL element.

Another situation in the advance phase is case ii shown in Fig. 3. As the elements on both sides of the node $\mathbf{x}_i$ are geometrically floating, the boundary condition imposed on $\mathbf{x}_i$ becomes $\chi(\mathbf{x}_i) = \sigma_{\mathbf{nn}}(\mathbf{x}_i) + p_w(\mathbf{x}_i) = 0$. However, the implicit treatment of the ice base moves the z-coordinate of the node $\mathbf{x}_i$ towards the bedrock with $u_{\mathbf{n}} > 0$ in Eq. (23) as discussed in Sect. 3.3. The result is that p_w defined by the implicit z_b in (23) satisfies $\sigma_{\mathbf{nn}} + p_w > 0$ in (27) and $\chi(\mathbf{x}_i) > 0$.

The implicit treatment of the ice base has the consequence that only case ii occurs in the *retreat phase*. When the FS equations are solved, the implicit update of the ice base with $u_{\mathbf{n}} < 0$ in Eq. (23) implies that the last grounded node in the previous time step is leaving the bedrock when the ice is retreating and the GL moves back to the adjacent element. Case i will not appear in that situation since $z_b(x_i) > b(x_i)$. In this circumstance, $\chi(\mathbf{x}_i) = 0$ in the floating node and a correction of $\chi(\mathbf{x})$ is introduced into case ii by $\tilde{\chi}$ in

$$\tilde{\chi}(\mathbf{x}) = \sigma_{\mathbf{nn}}(\mathbf{x}) + p_b(\mathbf{x}). \tag{29}$$

Here $p_b(\mathbf{x}) = -\rho_w g b(x)$ is the water pressure on the bedrock corresponding to linear extrapolation of the pressure for $x > x_{GL}$ along the element on the bedrock. Furthermore, $\tilde{\chi}(\mathbf{x}) \geq \chi(\mathbf{x})$. Notice that $p_b(\mathbf{x}_i) = p_w(\hat{\mathbf{x}}_i) > p_w(\mathbf{x}_i)$, where $\hat{\mathbf{x}}_i$ is a point on the bedrock with the same x coordinate of $\mathbf{x}_i$, as illustrated in the middle panel of Fig. 3. Both $\chi(\mathbf{x})$ in (27) and $\tilde{\chi}(\mathbf{x})$ in (29) are nonlinear in $\mathbf{x}$ but the numerical approximation of them will vary linearly in $\mathbf{x}$. A solution $\tilde{\mathbf{x}}_{GL}$ is found by linear interpolation of $\tilde{\chi}(\mathbf{x})$ between the nodes $\mathbf{x}_{i-1}$ and $\mathbf{x}_i$ as in Eq. (28). It follows from Eq. (28) that $\tilde{\mathbf{x}}_{GL}$ is located on the element boundary, see Figs. 2 and 3. If we compare with case i, this correction can be considered as using $\sigma_{\mathbf{nn}}(\tilde{\mathbf{x}}_{GL})$ to approximate $\sigma_{\mathbf{nn}}(\mathbf{x}_{GL})$ on a virtual element between $\mathbf{x}_{i-1}$ and $\hat{\mathbf{x}}_i$. The position $\tilde{\mathbf{x}}_{GL}$ is a numerical approximation of the analytical GL position, although it is not geometrically in contact with the bedrock.

Since we have $p_b(\mathbf{x}) = p_w(\mathbf{x})$ and $\chi(\mathbf{x}) = \tilde{\chi}(\mathbf{x})$ at the GL element in case i, we can simply use $\tilde{\chi}(\mathbf{x})$ to find $\tilde{\mathbf{x}}_{GL}$ for the two cases by replacing χ in (28) by $\tilde{\chi}$.

The domains Γ_{bg} and Γ_{bf} are separated at $\tilde{\mathbf{x}}_{GL}$ as in Eq. (15) and the integrals on the GL element are calculated with a high-order integration scheme as in Seroussi et al. (2014). We introduce two step functions $\mathcal{H}_{\mathcal{N}}(x)$ and $\mathcal{H}_{\beta}(x)$ to include and exclude quadrature points in the integration of Nitsche's term and the slip boundary condition, respectively. They are defined for case i in Fig. 2 and for case ii in Fig. 3. To achieve a reasonable numerical accuracy within the GL element, as suggested in Seroussi et al. (2014), at least tenth order Gaussian quadrature is used.

The penalty term in Nitsche's method restricts the motion of the element in the normal direction. It is only imposed on an element which is fully geometrically on the ground in case i. On the contrary in case ii, the GL element $\mathcal{E}_i$ is not in contact with the bedrock, see Fig. 3. The normal velocity on the element should not be forced to zero and only the floating boundary condition is then used on the GL element. Nitsche's penalty term should be imposed on all the fully geometrically

grounded elements and partially on the GL element in the advance phase as in case i. The step function $\mathcal{H}_\mathcal{N}(x)$ indicates how Nitsche's method is implemented on the basal elements, see the lower panels of Fig. 2 and 3 for the two cases. The penalty term contributes to the integration only when $\mathcal{H}_\mathcal{N}(x) = 1$.

The slip coefficient β is treated similarly with the step function $\mathcal{H}_\beta(x)$, where $\mathcal{H}_\beta(x) = 1$ is on the fully geometrically grounded elements and $\mathcal{H}_\beta(x) = 0$ on the floating elements. To further smooth the transition of β at the GL, the step function is set to be 1/2 in parts of the GL element before integrating using the high order scheme. In case i, full friction is applied at the grounded part between $\mathbf{x}_{i-1}$ and $\tilde{\mathbf{x}}_{GL}$ of the GL element since this part is also geometrically grounded in the analytical solution of the FS as in Fig. 2. Then, the friction is lower in the remaining part of $\mathcal{E}_i$. For the floating part between $\tilde{\mathbf{x}}_{GL}$ and $\mathbf{x}_i$ in case ii, there is no friction and $\mathcal{H}_\beta(x) = 0$ and we have reduced friction between $\mathbf{x}_{i-1}$ and $\tilde{\mathbf{x}}_{GL}$, see the lower panel of Fig. 3. The boundary integral Eq. (15) on $\mathcal{E}_i$ is now rewritten with the two step functions as

$$
\begin{aligned}
B_\Gamma + B_\mathcal{N} &= \int_{\mathcal{E}_i} -\mathcal{H}_\mathcal{N}(\sigma_{\mathbf{nn}}(\mathbf{u},p)\mathbf{n}\cdot\mathbf{v} + \sigma_{\mathbf{nn}}(\mathbf{v},q)\mathbf{n}\cdot\mathbf{u}) + \mathcal{H}_\beta\beta(\mathbf{t}\cdot\mathbf{u})(\mathbf{t}\cdot\mathbf{v}) + \mathcal{H}_\mathcal{N}\frac{\gamma_0}{h}(\mathbf{n}\cdot\mathbf{u})(\mathbf{n}\cdot\mathbf{v})\ \mathrm{d}s, \\
F_\Gamma &= \int_{\mathcal{E}_i} (1-\mathcal{H}_\mathcal{N})p_w\mathbf{n}\cdot\mathbf{v}\ \mathrm{d}s.
\end{aligned}
\tag{30}
$$

A summary of the numerical treatment of the GL is:

- Advance phase $\Rightarrow$ indicator χ in (27), case i or case ii
- Retreat phase $\Rightarrow$ indicator $\tilde{\chi}$ in (29), case ii

The case is determined by the geometry of the GL element and the sign of the indicator χ.

The algorithm for the GL element is:

Algorithm 3 Subgrid modeling for the GL element

Take all the 'potential GL elements' and solve $\chi(\mathbf{x}) = 0$ (advance phase) or $\tilde{\chi}(\mathbf{x}) = 0$ (retreat phase) to find $\tilde{x}_{GL}$ and the GL element.
Determine which case this GL element belongs to by checking the geometrical conditions at $\mathbf{x}_i$.
Specify $\mathcal{H}_\mathcal{N}(x)$ and $\mathcal{H}_\beta(x)$ based on $\tilde{x}_{GL}$ depending on the case and the advance or retreat phase.
Integrate Eq. (30) for the FEM matrix assembly.

Equations (1), (7), and (8) form a system of coupled nonlinear equations. They are solved in the same manner as in Elmer/ICE v.8.3. The detailed procedure is explained in Algorithms 1, 2, and 3. The solution to the nonlinear FS system is computed with Picard iterations to a 10^{-5} relative error with a limit of maximal 25 nonlinear iterations. The $\tilde{\mathbf{x}}_{GL}$ position is determined dynamically during each fixed-point iteration by solving Eq. (28) with χ or $\tilde{\chi}$ and the solution $\sigma_{\mathbf{nn}}(\mathbf{x})$ from the previous nonlinear iteration, and the step functions $\mathcal{H}_\mathcal{N}$ and $\mathcal{H}_\beta$ are adjusted accordingly. The water pressure p_b is fixed since the ice geometry is not changed during the nonlinear iterations.

5 Results

The numerical experiments follow the MISMIP benchmark (Pattyn et al., 2012) and a comparison is made with the results in Gagliardini et al. (2016). Using the experiment MISMIP 3a, the setups are exactly the same as in the advancing and retreating simulations in Gagliardini et al. (2016). The experiments are run with spatial resolutions of $\Delta x = 4$ km, 2 km, 1 km and 0.5 km. The mesh at the base is extruded vertically in 20 layers with equidistantly placed nodes in each vertical column. The time step is $\Delta t = 0.125$ year for all four resolutions to eliminate time discretization errors when comparing different spatial resolutions.

The dependence on γ_0 in (30) for the retreating ice is shown in Fig. 4 with γ_0 between 10^4 and 10^9. The estimated GL positions do not vary with different choices of γ_0 from 10^5 to 10^8 which suggests a suitable range of γ_0. If γ_0 is too small ($\gamma_0 \ll 10^4$), oscillations appear in the estimated GL positions. If γ_0 is too large ($\gamma_0 \gg 10^8$), then more nonlinear iterations in Algorithm 1 are needed in each time step. The same dependency of γ_0 is observed for the advancing experiments and for different mesh resolutions as well. The results are not very sensitive to γ_0 and for the remaining experiments we choose $\gamma_0 = 10^6$.

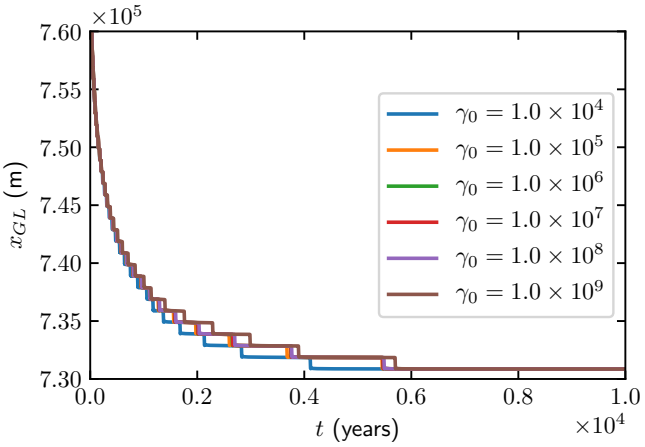

Figure 4. The MISMIP 3a retreat experiment with $\Delta x = 1$ km for different choices of γ_0 in the time interval $[0, 10000]$ years.

The GL position during the transient simulations in the advance and retreat phases are displayed in Fig. 5 and the steady state results (at $t = 10000$) are shown in Fig. 6 for different mesh resolutions. The range of the steady state solutions from Gagliardini et al. (2016) with mesh resolution from 25 m to 200 m are shown as background shaded regions in red. We achieve similar GL migration results for both the advance and retreat experiments with at least 20 times larger mesh resolutions. The GL position is insensitive to the variation in mesh size between 0.5 km and 4 km.

The distance between the steady state GL positions of the retreat and the advance phases is shown in Fig. 6 (b). The maximal distance is about 6 km at $\Delta x = 1$ km with the subgrid model, whereas in Gagliardini et al. (2016), the resolution has to be below 50 m to achieve a similar result.

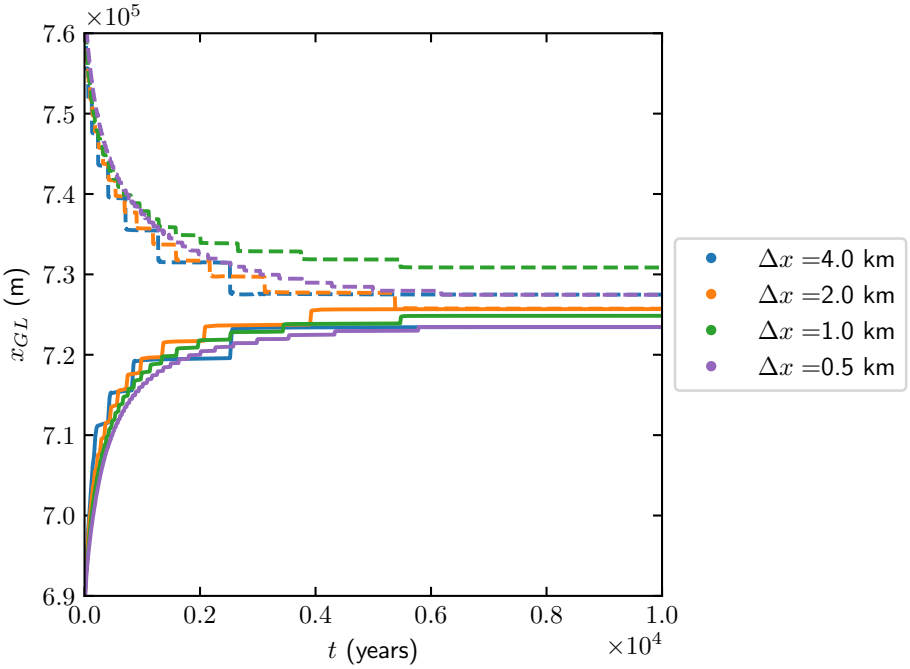

Figure 5. The MISMIP 3a experiments for the GL position when $t \in [0, 10000]$ with $\Delta x = 4$ km, 2 km, 1 km and 0.5 km for the advance (solid) and retreat (dashed) phases.

We observed oscillations at the ice surface near the GL in all the experiments as expected from Durand et al. (2009a); Schoof (2011). A zoom-in plot of the surface elevation with $\Delta x = 0.5$ km at $t = 10000$ years is found to the left in Fig. 7, where the red dashed line indicates the estimated GL position.

The ratio between the thickness below sea level H_{bw} and the ice thickness H is shown to the right in Fig. 7. The horizontal, purple, dash-dotted line represents the ratio of ρ/ρ_w and the estimated GL is located at the red, dashed line. This result confirms that the hydrostatic assumption $H\rho = H_{bw}\rho_w$ in Eq. (9) is not valid in the FS equations for $x > x_{GL}$ close to the GL and at the GL position, cf. Durand et al. (2009a); Schoof (2011). For $x < x_{GL}$ we have that $H_{bw}/H < \rho/\rho_w$ since H_{bw} decreases and H increases. The conclusion from numerical experiments in van Dongen et al. (2018) is that the hydrostatic assumption and the SSA equations approximate the FS equations well for the floating ice beginning at a short distance away from the GL.

The solution varies smoothly over the mesh and $\Delta x = 0.5$ km appears to be a sufficient resolution in both panels of Fig. 7. In general, the estimated GL position does not coincide with any nodes even at the steady state but it may be close to a node.

The surface and the base velocity solutions from the retreat experiment are displayed in Fig. 8 with $\Delta x = 0.5$ km after 10000 years. The horizontal velocities on the two surfaces are similar with negligibly small differences on the floating ice as expected. The vertical velocities w on the surface (orange line) and the base (blue line) at the GL are almost discontinuous as analyzed in Schoof (2011). With the subgrid model, the rapid variation is captured on the 0.5 km mesh size.

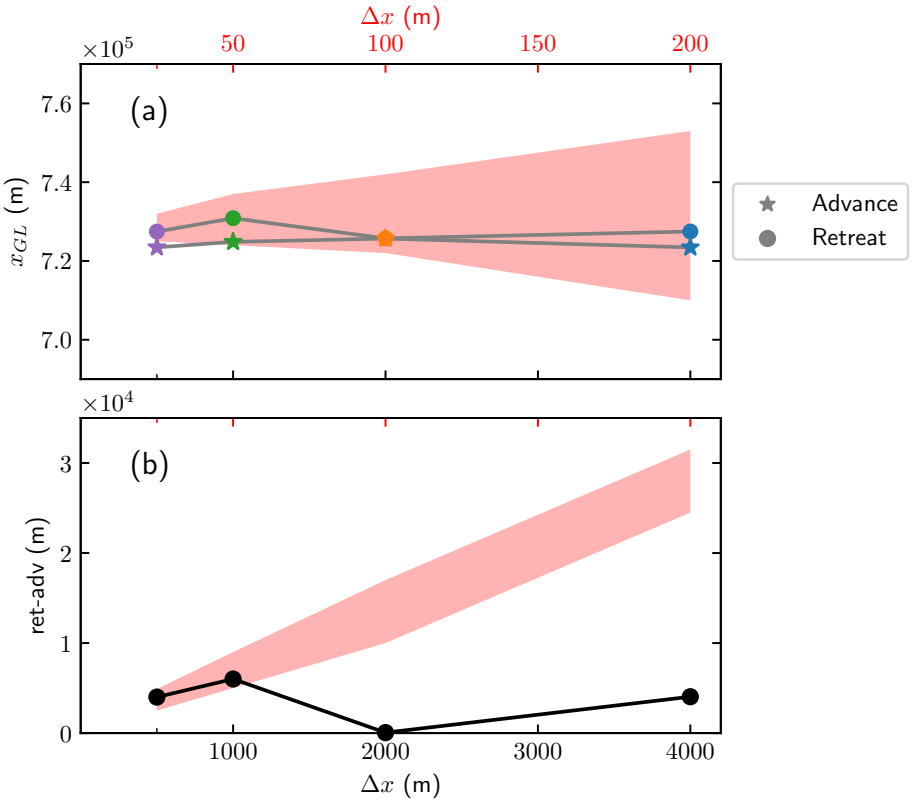

Figure 6. The MISMIP 3a experiments at the final time $t = 10000$ with the resolutions at $\Delta x = 4$ km, 2 km, 1 km and 0.5 km. (a) The GL positions in the advance (★) and retreat (•) phases. (b) The distance between the retreat and the advance x_{GL} at the steady states. The shaded regions indicate the range of the results in Gagliardini et al. (2016) with *20 times smaller mesh resolutions* from 25 to 200 m with the axis scale shown in red at the top of the plot.

6 Discussion

Seroussi et al. (2014) describe four different subgrid models (NSEP, SEP1, SEP2 and SEP3) for the friction in SSA and evaluate them in a FEM discretization on a triangulated, planar domain. The flotation criterion is applied at the nodes of the triangles. In the NSEP, an element is floating or not depending on how many of the nodes that are floating. In the other three methods, an inner structure in the triangular element is introduced. One part of a triangle is floating and one part is grounded. The amount of friction in a triangle with the GL is determined by the flotation criterion. Either the friction coefficient is reduced, the integration in the element only includes the grounded part, or a higher order polynomial integration (SEP3) is applied. Faster convergence as the mesh is refined is observed for the latter methods compared to the first method. The discretization of the friction in Sect. 4 is similar to the SEP3 method but the FS equations also require a subgrid treatment of the normal velocity condition. In the method for the FS equations in Gagliardini et al. (2016), the GL position is in a node and the friction

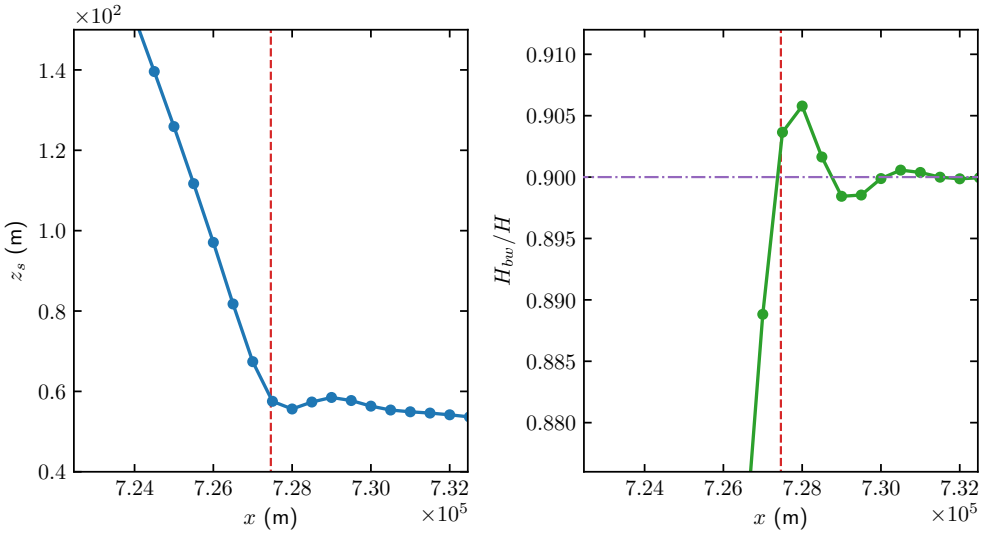

Figure 7. Details of the solutions for the retreat experiment with $\Delta x = 0.5$ km after 10000 years. The solid dots represent the nodes of the elements and the vertical, red, dashed lines indicate the GL position. *Left panel*: The oscillations at ice surface near GL. *Right panel*: The flotation criterion is evaluated by H_{bw}/H. The ratio between ρ/ρ_w is drawn in a horizontal, purple, dash-dotted line.

coefficient is approximated in three different ways. The coefficient is discontinuous at the node in one case (DI in Gagliardini et al. (2016)). Our coefficient is also discontinuous but at the estimated location of the GL between the nodes.

The convergence of the steady state GL position toward the reference solutions in Gagliardini et al. (2016) is observed in the simulations in Fig. 5 and 6. However, as the meshes we used are at least 20 times larger than the 25 m finest resolution in Gagliardini et al. (2016), it is still far from the convergence asymptote. At the current resolutions, the discretization introduces a strong mesh effect such as the two different geometrical interpretations in the two cases mentioned in Sect. 4. The subgrid scheme is able to provide a more accurate representation of the GL position and the boundary conditions, but the numerical solution of the velocity field, pressure as well as the two free surfaces are still computed on the coarse mesh, which are the main sources of the numerical errors. Additional uncertainty at the GL is introduced by the approximation of the bedrock geometry, the friction at the GL, and the modeling of the ice/ocean interaction. It is shown in Cheng and Lötstedt (2020) that the solution at the GL is particularly sensitive to variation in the geometry and friction at the ice base.

Our method can be extended to a triangular mesh covering Γ_b in the following way (considering linear Lagrange functions). The condition on χ in Eq. (27) or $\tilde{\chi}$ in Eq. (29) is applied on the edges of each triangle $\mathcal{T}$ in the mesh. If $\chi < 0$ in all three nodes then $\mathcal{T}$ is grounded. If $\chi \geq 0$ in all nodes then $\mathcal{T}$ is floating. The GL passes inside $\mathcal{T}$ if χ has a different sign in one of the nodes. Then the GL crosses the two edges where $\chi < 0$ in one node and $\chi \geq 0$ in the other node. In this way, a continuous reconstruction of a piecewise linear GL is possible on Γ_b. The same tests are applied to $\tilde{\chi}$. The FEM approximation is modified in the same manner as in Sect. 4 using step functions in Nitsche's method.

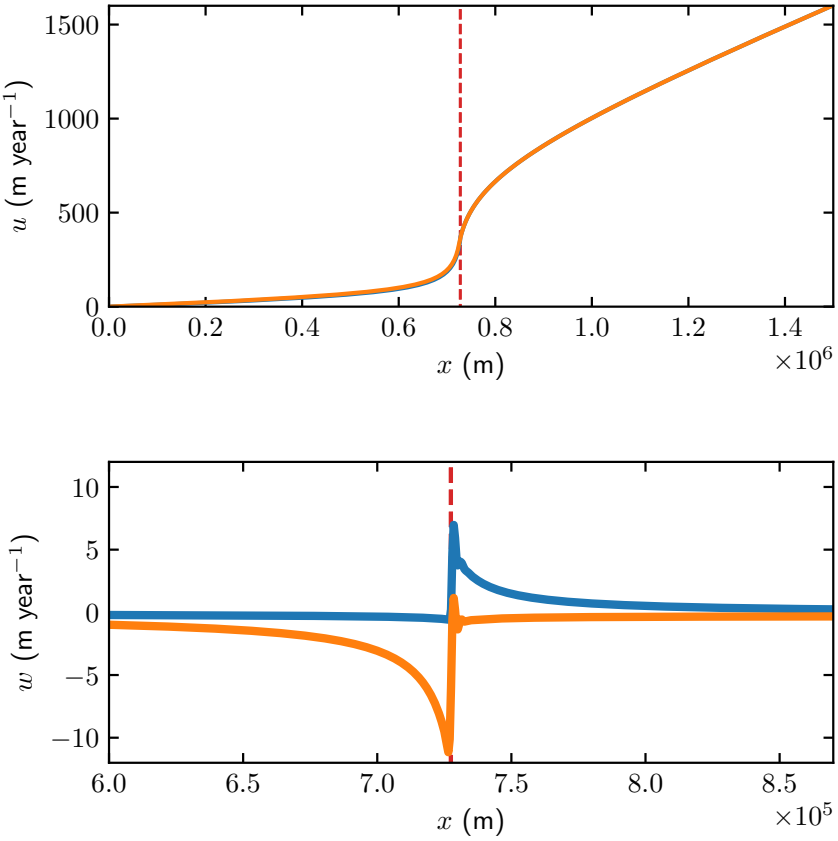

Figure 8. The velocities u (upper panel) and w (lower panel) on the surface (orange) and the base (blue) of the ice in the retreat experiment with $\Delta x = 0.5$ km after 10000 years. The red, dashed line marks the GL position. The vertical velocity w is zoomed-in close to the GL.

An alternative to a subgrid scheme is to introduce static or dynamic adaptation of the mesh on Γ_b with a refinement at the GL as in e.g. Gladstone et al. (2010a); Cornford et al. (2013); Drouet et al. (2013). In general, a fine mesh is needed at the GL and in an area surrounding it. Since the GL moves long distances in simulations of palaeo-ice sheets, the adaptation should be dynamic, permit refinement and coarsening of the mesh varying in time, and be based on some estimate of the numerical error of the method. In shorter time intervals, a static adaptation may be sufficient since the GL will move a shorter distance. Furthermore, shorter time steps are necessary for numerical stability in static and dynamic mesh adaptation schemes. A static adaptation is determined once before the simulation starts. Introducing a time dependent, dynamic mesh adaptivity into an existing code requires a substantial coding effort and will increase the computational work considerably. Subgrid modeling is easier to implement and the increase in computing time is small. A combination of dynamic mesh adaptation and subgrid discretization may be the ultimate solution.

7 Conclusions

A subgrid scheme at the GL has been developed and tested in the SSA model for 2D vertical ice flow in Gladstone et al. (2010b) and in Seroussi et al. (2014), for the friction in the vertically integrated model BISICLES (Cornford et al., 2013) for 2D flow in Cornford et al. (2016), and for the PISM model mixing SIA with SSA in 3D in Feldmann et al. (2014). Here we propose a subgrid scheme for the FS equations for a 2D vertical ice, implemented in Elmer/ICE, that can be extended to 3D. The mesh is static and the moving GL position within one element is determined by linear interpolation with an auxiliary function $\chi(\mathbf{x})$ or $\tilde{\chi}(\mathbf{x})$. Only in that element, the FEM discretization is modified to accommodate the discontinuities in the boundary conditions.

The numerical scheme is applied to the simulation of a 2D vertical ice sheet with an advancing GL and one with a retreating GL. The model setups for the tests are the same as in one of the MISMIP examples (Pattyn et al., 2012) and in Gagliardini et al. (2016). Comparable results to Gagliardini et al. (2016) are obtained using the subgrid scheme with more than 20 times larger mesh sizes. A larger mesh size also allows a longer time step for the time integration.

Code availability. The FS sub-grid model is implemented based on Elmer/ICE Version: 8.3 (Rev: f6bfdc9) with the scripts at http://doi.org/10.5281/zenodo.3401478 and http://doi.org/10.5281/zenodo.3401475.

Author contributions. GC developed the model code and performed the simulations. GC and PL contributed to the theory of the paper. GC, PL and LvS contributed to the development of the method and the writing of the paper

Competing interests. The authors declare that they have no conflict of interest.

Acknowledgements. This work has been supported by Nina Kirchner's Formas grant 2017-00665 and the Swedish e-Science initiative eSSENCE. We are grateful to Thomas Zwinger for advise and help in the implementation of the subgrid scheme in Elmer/ICE. The computations were performed on resources provided by the Swedish National Infrastructure for Computing (SNIC) at the PDC Center for High Performance Computing, KTH Royal Institute of Technology. We also thank the anonymous referees for their helpful comments.

References

Brondex, J., Gagliardini, O., Gillet-Chaulet, F., and Durand, G.: Sensitivity of grounding line dynamics to the choice of the friction law, J. Glaciology, 63, 854–866, 2017.

Chen, Q., Gunzburger, M., and Perego, M.: Well-posedness results for a nonlinear Stokes problem arising in glaciology, SIAM Journal on Mathematical Analysis, 45, 2710–2733, 2013.

Cheng, G. and Lötstedt, P.: Parameter sensitivity analysis of dynamic ice sheet models-numerical computations, Cryosphere, 14, 673–691, 2020.

Cheng, G., Lötstedt, P., and von Sydow, L.: Accurate and stable time stepping in ice sheet modeling, Journal of Computational Physics, 329, 29–47, 2017.

Chouly, F., Fabre, M., Hild, P., Mlika, R., Pousin, J., and Renard, Y.: An overview of recent results on Nitsche's method for contact problems, in: Geometrically unfitted finite element methods and applications, pp. 93–141, Springer, 2017a.

Chouly, F., Hild, P., Lleras, V., and Renard, Y.: Nitsche-based finite element method for contact with Coulomb friction, in: European Conference on Numerical Mathematics and Advanced Applications, pp. 839–847, Springer, 2017b.

Christensen, P. W., Klarbring, A., Pang, J. S., and Strömberg, N.: Formulation and comparison of algorithms for frictional contact problems, Int. J. Num. Meth. Eng., 42, 145–173, 1998.

Cornford, S., Martin, D., Lee, V., Payne, A., and Ng, E.: Adaptive mesh refinement versus subgrid friction interpolation in simulations of Antarctic ice dynamics, Ann. Glaciol., 57, 1–9, 2016.

Cornford, S. L., Martin, D. F., Graves, D. T., Ranken, D. F., Brocq, A. M. L., Gladstone, R. M., Payne, A. J., Ng, E. G., and Lipscomb, W. H.: Adaptive mesh, finite volume modeling of marine ice sheets, J. Comput. Phys., 232, 529–549, 2013.

DeConto, R. M. and Pollard, D.: Contribution of Antarctica to past and future sea-level rise, Nature, 531, 591–597, 2016.

Docquier, D., Perichon, L., and Pattyn, F.: Representing grounding line dynamics in numerical ice sheet models: Recent advances and outlook, Surv. Geophys., 32, 417–435, 2011.

van Dongen, E. C. H., Kirchner, N., van Gijzen, M. B., van de Wal, R. S. W., Zwinger, T., Cheng, G., Lötstedt, P., and von Sydow, L.: Dynamically coupling full Stokes and shallow shelf approximation for marine ice sheet flow using Elmer/ICE (v8. 3), Geoscientific Model Development, 11, 4563–4576, 2018.

Drouet, A. S., Docquier, D., Durand, G., Hindmarsh, R., Pattyn, F., Gagliardini, O., and Zwinger, T.: Grounding line transient response in marine ice sheet models, Cryosphere, 7, 395–406, 2013.

Durand, G. and Pattyn, F.: Reducing uncertainties in projections of Antarctic ice mass loss, Cryosphere, 9, 2043–2055, 2015.

Durand, G., Gagliardini, O., de Fleurian, B., Zwinger, T., and Le Meur, E.: Marine ice sheet dynamics: Hysteresis and neutral equilibrium, J. Geophys. Res.: Earth Surf., 114, F03 009, 2009a.

Durand, G., Gagliardini, O., Zwinger, T., Le Meur, E., and Hindmarsh, R. C. A.: Full Stokes modeling of marine ice sheets: influence of the grid size, Ann. Glaciol., 50, 109–114, 2009b.

Feldmann, J., Albrecht, T., Khroulev, C., Pattyn, F., and Levermann, A.: Resolution-dependent performance of grounding line motion in a shallow model compared with a full-Stokes model according to the MISMIP3d intercomparison, J. Glaciol., 60, 353–360, 2014.

Franca, L. P. and Frey, S. L.: Stabilized finite element methods: II. The incompressible Navier-Stokes equations, Computer Methods in Applied Mechanics and Engineering, 99, 209–233, 1992.

Gagliardini, O., Zwinger, T., Gillet-Chaulet, F., Durand, G., Favier, L., de Fleurian, B., Greve, R., Malinen, M., Martín, C., Råback, P., Ruokolainen, J., Sacchettini, M., Schäfer, M., Seddik, H., and Thies, J.: Capabilities and performance of Elmer/Ice, a new generation ice-sheet model, Geosci. Model Dev., 6, 1299–1318, 2013.

Gagliardini, O., Brondex, J., Gillet-Chaulet, F., Tavard, L., Peyraud, V., and Durand, G.: On the substantial influence of the treatment of friction at the grounding line, Cryosphere, 9, 3475–3501, 2015.

Gagliardini, O., Brondex, J., Gillet-Chaulet, F., Tavard, L., Peyaud, V., and Durand, G.: Impact of mesh resolution for MISMIP and MISMIP3d experiments using Elmer/ICE, The Cryosphere, 10, 307–312, 2016.

Gladstone, R. M., Lee, V., Vieli, A., and Payne, A. J.: Grounding line migration in an adaptive mesh ice sheet model, J. Geophys. Res., 115, F04 014, 2010a.

Gladstone, R. M., Payne, A. J., and Cornford, S. L.: Parameterising the grounding line in flow-line ice sheet models, Cryosphere, 4, 605–619, 2010b.

Gladstone, R. M., Warner, R. C., Galton-Fenzi, B. K., Gagliardini, O., Zwinger, T., and Greve, R.: Marine ice sheet model performance depends on basal sliding physics and sub-shelf melting, Cryosphere, 11, 319–329, 2017.

Gong, Y., Zwinger, T., Cornford, S., Gladstone, R., Schäfer, M., and Moore, J. C.: Importance of basal boundary conditions in transient simulations: case study of a surging marine-terminating glacier on Austfonna, Svalbard, J. Glaciol., 63, 106–117, 2017.

Hanna, E., Navarro, F. J., Pattyn, F., Domingues, C. M., Fettweis, X., Ivins, E. R., Nicholls, R. J., Ritz, C., Smith, B., Tulaczyk, S., Whitehouse, P. L., and Zwally, H. J.: Ice-sheet mass balance and climate change, Nature, 498, 51–59, 2013.

Helanow, C. and Ahlkrona, J.: Stabilized equal low-order finite elements in ice sheet modeling–accuracy and robustness, Computational Geosciences, 22, 951–974, 2018.

Hutter, K.: Theoretical Glaciology, D. Reidel Publishing Company, Terra Scientific Publishing Company, Dordrecht, 1983.

Jouvet, G. and Rappaz, J.: Analysis and finite element approximation of a nonlinear stationary Stokes problem arising in glaciology, Adv. Numer. Anal., 2011, 164 581, 2011.

Kingslake, J., Scherer, R. P., Albrecht, T., Coenen, J., Powell, R. D., Reese, R., Stansell, N. D., Tulaczyk, S., Wearing, M. G., and Whitehouse, P. L.: Extensive retreat and re-advance of the West Antarctic ice sheet during the Holocene, Nature, 558, 430–434, 2018.

Konrad, H., Shepherd, A., Gilbert, L., Hogg, A. E., McMillan, M., Muir, A., and Slater, T.: Net retreat of Antarctic glacier grounding line, Nat. Geosci., 11, 258–262, 2018.

Larour, E., Seroussi, H., Adhikari, S., Ivins, E., Caron, L., Morlighem, M., and Schlegel, N.: Slowdown in Antarctic mass loss from solid Earth and sea-level feedbacks, Science, 364, eaav7908, 2019.

Leguy, G. R., Asay-Davis, X. S., and Lipscomb, W. H.: Parameterization of basal friction near grounding lines in a one-dimensional ice sheet model, Cryosphere, 8, 1239–1259, 2014.

Leng, W., Ju, L., Gunzburger, M., Price, S., and Ringler, T.: A parallel high-order accurate finite element nonlinear Stokes ice sheet model and benchmark experiments, J. Geophys. Res.: Earth Surf., 117, 2156–2202, 2012.

MacAyeal, D. R.: Large-scale ice flow over a viscous basal sediment: Theory and application to Ice Stream B, Antarctica., J. Geophys. Res., 94, 4071–4078, 1989.

Martin, N. and Monnier, J.: Four-field finite element solver and sensitivities for quasi-Newtonian flows, SIAM Journal on Scientific Computing, 36, S132–S165, 2014.

Nitsche, J.: Über ein Variationsprinzip zur Lösung von Dirichlet-Problemen bei Verwendung von Teilräumen, die keinen Randbedingungen unterworfen sind, Abh. Math. Semin., University of Hamburg, Germany, 36, 9–15, 1971.

Nowicki, S. M. J. and Wingham, D. J.: Conditions for a steady ice sheet–ice shelf junction, Earth Plan. Sci. Lett., 265, 246–255, 2008.

Pattyn, F. and Durand, G.: Why marine ice sheet model predictions may diverge in estimating future sea level rise, Geophys. Res. Lett., 40, 4316–4320, 2013.

Pattyn, F., Schoof, C., Perichon, L., Hindmarsh, R. C. A., Bueler, E., de Fleurian, B., Durand, G., Gagliardini, O., Gladstone, R., Goldberg, D., Gudmundsson, G. H., Huybrechts, P., Lee, V., Nick, F. M., Payne, A. J., Pollard, D., Rybak, O., Saito, F., and Vieli, A.: Results of the Marine Ice Sheet Model Intercomparison Project, MISMIP, Cryosphere, 6, 573–588, 2012.

Pattyn, F., Perichon, L., Durand, G., Favier, L., Gagliardini, O., Hindmarsh, R. C. A., Zwinger, T., Albrecht, T., Cornford, S., Docquier, D., Fürst, J. J., Goldberg, D., Gudmundsson, G. H., Humbert, A., Hütten, M., Jouvet, G., Kleiner, T., Larour, E., Martin, D., Morlighem, M., Payne, A. J., Pollard, D., Rückamp, M., Rybak, O., Seroussi, H., Thoma, M., and Wilkens, N.: Grounding-line migration in plan-view marine ice-sheet models: results of the ice2sea MISMIP3d intercomparison, J. Glaciol., 59, 410–422, 2013.

Reusken, A., Xu, X., and Zhang, L.: Finite element methods for a class of continuum models for immiscible flows with moving contact lines, Int. J. Numer. Meth. Fluids, 84, 268–291, 2017.

Schoof, C.: Marine ice sheet dynamics. Part 2. A Stokes flow contact problem, J. Fluid Mech., 679, 122–155, 2011.

Schoof, C. and Hindmarsh, R.: Thin-Film Flows with Wall Slip: An Asymptotic Analysis of Higher Order Glacier Flow Models, Quart. J. Mech. Appl. Math., 63, 73–114, 2010.

Seroussi, H., Morlighem, M., Larour, E., Rignot, E., and Khazendar, A.: Hydrostatic grounding line parameterization in ice sheet models, Cryosphere, 8, 2075–2087, 2014.

Stokes, C. R., Tarasov, L., Blomdin, R., Cronin, T. M., Fisher, T. G., Gyllencreutz, R., Hättestrand, C., Heyman, J., Hindmarsh, R. C. A., Hughes, A. L. C., Jakobsson, M., Kirchner, N., Livingstone, S. J., Margold, M., Murton, J. B., Noormets, R., Peltier, W. R., Peteet, D. M., Piper, D. J. W., Preusser, F., Renssen, H., Roberts, D. H., Roche, D. M., Saint-Ange, F., and Stroeven, A. P.: On the reconstruction of palaeo-ice sheets: Recent advances and future challenges, Quat. Sci. Rev., 125, 15–49, 2015.

Urquiza, J. M., Garon, A., and Farinas, M.-I.: Weak imposition of the slip boundary condition on curved boundaries for Stokes flow, J. Comput. Phys., 256, 748–767, 2014.

Wilchinsky, A. V. and Chugunov, V. A.: Ice-stream–ice-shelf transition: theoretical analysis of two-dimensional flow, Ann. Glaciology, 30, 153–162, 2000.

Zhang, T., Price, S., Ju, L., Lei, W., Brondex, J., Durand, G., and Gagliardini, O.: A comparison of two Stokes ice sheet models applied to the Marine Ice Sheet Model Intercomparison Project for plan view models, Cryosphere, 11, 179–190, 2017.